

² Muon Track Reconstruction in a Segmented Bolometric ³ Array Using Multi-Objective Optimization

⁴ **J. Yocom,¹ D. Mayer, J. L. Ouellet, and L. Winslow**

⁵ *Laboratory for Nuclear Science, Massachusetts Institute of Technology, Cambridge, MA 02139, USA*

⁶ *E-mail: juliany@mit.edu, lwinslow@mit.edu*

⁷ **ABSTRACT:** Recent advances in segmented solid-state detector arrays for rare-event searches have
⁸ allowed the technology to approach the ton-scale in detector mass and the scale of meters in size.
⁹ Often focused around searches for neutrinoless double-beta decay or direct dark matter detection,
¹⁰ such experiments also have the capability to search for exotic particles that leave track-like signatures
¹¹ across their volume. However, the segmented nature of such detector arrays often sets the spatial
¹² resolution and makes the problem of reconstructing track-like paths non-trivial. In this paper, we
¹³ present an algorithm that improves reconstruction of track-like events in segmented detectors using
¹⁴ multi-objective optimization – a computational technique that optimizes more than one cost function
¹⁵ at a time without specifying a quantitative weighting between them. Such a technique allows the
¹⁶ reconstruction of tracks through a detector and the determination of path-lengths through individual
¹⁷ elements. When combined with the reconstructed energy depositions in each element this allows
¹⁸ for a calculation of the stopping power of track-like particles and opens the door to searches for
¹⁹ particles with abnormal stopping power like monopoles or lightly-ionizing particles (LIPs). Results
²⁰ are presented which evaluate the precision of the reconstruction tools as they currently stand against
²¹ Monte Carlo generated data. The algorithm is presented in the context of the CUORE experiment,
²² but has applications to other segmented calorimeter detectors.

²³ **KEYWORDS:** Analysis and statistical methods; Data processing methods; Pattern recognition, cluster
²⁴ finding, calibration and fitting methods; Double-beta decay detectors; Dark Matter detectors;
²⁵ Calorimeters; Cryogenic detectors; Bolometers for dark matter research;

¹Corresponding author.

| | | |
|----|---|----|
| 26 | Contents | |
| 27 | 1 Introduction | 1 |
| 28 | 2 The CUORE Detector | 2 |
| 29 | 3 Multi-Objective Optimization | 4 |
| 30 | 4 Simulation of Muon Tracks | 6 |
| 31 | 5 Algorithm Performance on Muon Tracks | 8 |
| 32 | 6 Discussion | 10 |

33 **1 Introduction**

34 Track-like event topologies are no stranger to particle detectors. Muon tracks within cloud chambers
35 were one of the first direct observations of particle interactions. In recent years, segmented arrays
36 of large solid-state detectors searching for neutrinoless double beta decay ($0\nu\beta\beta$ decay), dark
37 matter, or other rare-events have reached suitable sizes so as to enable particle tracking across
38 their volume. Despite their smaller exposures in terms of area-steradian coverage compared to
39 traditional large-volume liquid or plastic scintillators or gaseous trackers, such contemporary solid-
40 state detectors benefit from high energy resolution and low dE/dx thresholds. Combined with their
41 typical placement in deep underground labs, this can result in competitive sensitivity to exotic track-
42 like phenomena including multiply-interacting dark matter [1] and lightly-ionizing particles (LIPs)
43 [2, 3]. Conversely, as the background requirements of these rare-event searches become increasingly
44 stringent, it is valuable to have a precise *in situ* characterization of cosmogenic backgrounds such
45 as muon-induced spallation products [4–6]. Either in tandem with dedicated muon-veto detector
46 systems or as a stand-alone reconstruction, precise tracking information of muons crossing the
47 detector volume can enable data-driven studies of these backgrounds.

48 However, as these segmented detector arrays were not designed for particle tracking, many of
49 their features make precise track reconstruction difficult. Chief among these are poor spatial and
50 temporal resolution. In rare event searches, many radioactive backgrounds are distributed on the
51 surfaces of detector modules, while sensitivity scales with the module volume. As a result, rare-
52 event searches tend to opt for arrays of large detector modules with large volume-to-surface ratios.
53 The detectors have poor spatial resolution (of the order of several cm) and poor timing resolution (of
54 the order of 10’s of μ s to 100’s of ms). For such detector arrays, it is imperative to exploit as much
55 geometric information as possible when reconstructing detector-wide events in order to maximize
56 the physics reach. Potential searches for new physics, along with in-depth cosmogenic background
57 characterization, motivate the development of track reconstruction algorithms tailor-made for these
58 segmented solid-state detectors.

59 In this paper, we present an algorithm using multi-objective optimization for the purpose of
60 reconstructing track-like events within a large segmented solid-state detector array with low spatial
61 and temporal resolution. Multi- and many-objective optimization techniques allow for one to
62 find solutions to problems which must simultaneously extremize over multiple objective functions
63 without needing to specify weights *a priori*. The algorithm presented here is implemented using
64 the `pymoo` library, with objective functions and problem constraints chosen to reflect the physics
65 of track-like energy depositions within the geometry of the existing CUORE detector. Though the
66 algorithm presented here can be applied to any particle (Standard Model or beyond) that leaves a
67 linear track, we will mainly focus on muons throughout this paper as they are the most common
68 expected track-like interaction in CUORE.

69 2 The CUORE Detector

70 The Cryogenic Underground Observatory for Rare Events (CUORE) is a ton-scale cryogenic de-
71 tector searching for $0\nu\beta\beta$ decay in ^{130}Te [7–9]. Situated within the Laboratori Nazionali del Gran
72 Sasso (LNGS), the detector is composed of 988 high-purity 5 cm×5 cm×5 cm TeO_2 crystals, each
73 instrumented as a macroscopic cryogenic calorimeter. The crystals are arranged into 19 towers of
74 13 floors each, providing a segmented geometry which allows for the reconstruction of energy depo-
75 sitions occurring within multiple crystals and across the detector (see Fig. 1). An energy deposition
76 in any crystal leads to a sudden rise in temperature (on the order of 100 $\mu\text{K}/\text{MeV}$) [9], which can
77 be triggered and used to extract the energy deposited. Each crystal is operated independently, but
78 can be combined offline to look for simultaneous energy depositions across multiple calorimeters.

79 The detector is housed within the CUORE cryostat [10] and held at a temperature of approxi-
80 mately 12 mK. Ancient roman lead shielding within the cryostat efficiently blocks external gamma
81 rays from reaching active detector components, while stringent materials screening and selection
82 during CUORE’s construction serve to reduce intrinsic radiogenic backgrounds. CUORE has col-
83 lected more than $1000 \text{ kg} \cdot \text{yr}$ in exposure, to-date the largest exposure of a cryogenic solid-state
84 based detector.

85 Each crystal in CUORE is thermally isolated, save for a weak thermal link to a cold bath at
86 $\approx 12 \text{ mK}$, and a neutron transmutation doped (NTD) thermistor [12], which acts as a sensitive
87 thermometer. Energy depositions within the crystal will yield a heat deposition, which is read out
88 as a voltage pulse on the NTD with risetimes of $\sim 50 \text{ ms}$ and falltimes of $\sim 1 \text{ s}$. The voltage from
89 each calorimeter is digitized at 1 kS/s and stored to disk as a continuous waveform. Pulses are
90 triggered offline using an optimum-filter based trigger [13, 14], and are analyzed to extract the pulse
91 amplitude, stabilize against thermal gain drifts, and calibrate the amplitude into an estimate of the
92 deposited energy [15]. During physics data taking, individual crystals have typical trigger rates of
93 a few mHz.

94 Finally, pulses are time-correlated and classified according to their multiplicity, that is the
95 number of calorimeters which are found to have triggered in coincidence with each other. The
96 typical timing resolution of two simultaneous energy depositions is on the order of 5-10 ms. Track-
97 like muons within CUORE may be expected to give rise to multiplicities between 1 to ~ 20 , depending
98 on their geometric intersection across the detector. The long thermal timescales involved in the
99 calorimetric technique are unable to resolve time-of-flight measurements for relativistic particles

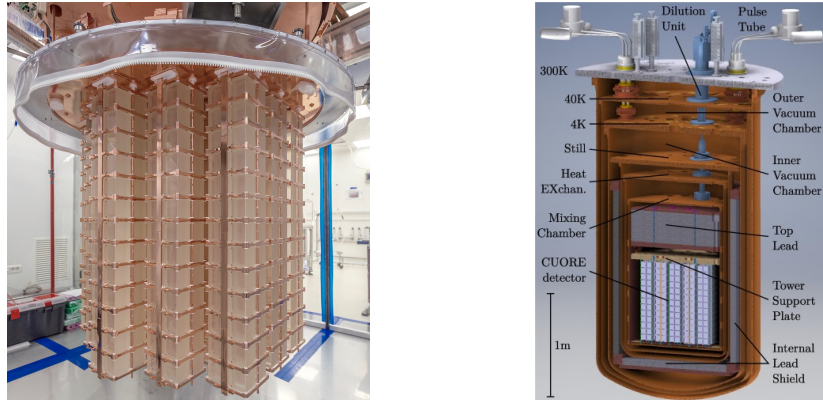


Figure 1: *Left:* The CUORE detector suspended from the CUORE cryostat during detector installation. The crystal absorbers are suspended in copper frames in a 19-tower, 13-floor array. *Right:* A schematic of the CUORE detector inside the CUORE cryostat. The detector is surrounded by nested layers of copper thermal shielding and lead γ shielding. An additional 24 cm thick lead shield (not pictured) surrounds the bottom and sides of the cryostat. Figures from [10, 11].

traversing the detector. Practically, all prompt events induced by a given muon within CUORE will appear simultaneous, up to the timing resolution [16]. Nonetheless, the low background rates within the detector lead to >90% of muon tracks being free from pile-up with accidental coincidences within the detector.

As CUORE is optimized for its energy resolution about the $Q_{\beta\beta}$ -value for ^{130}Te of 2.528 MeV [17–19], single-crystal depositions of $\gtrsim 20$ MeV are found to saturate the digitizer dynamic range. As muons can deposit energies well above this range, this presents a challenge for muon reconstruction algorithms which rely on the reconstructed energy. Future efforts may seek to recover such saturated pulses, through the use of the leading and trailing edges of the pulse in conjunction with the known thermal response. Conversely, energy depositions close to a calorimeter’s trigger threshold may fail to generate an event and could result in energy missing from a track. While this may become important in searches for exotic particles, it is rarely a problem for muons, which tend to leave energy depositions well over the trigger thresholds, even as minimum ionizing particles.

The large overburden provided by LNGS attenuates the vast majority of the cosmic muon flux. The surviving flux has been measured to be $\Gamma \approx (3.2 \pm 0.2) \times 10^{-8} \mu \cdot \text{s}^{-1} \cdot \text{cm}^{-2}$ [20, 21], which implies a muon interaction rate in CUORE of approximately 1 per hour [22]. The distribution of muons is peaked about the vertical, with almost no flux with zenith angle $\cos \theta < 0.4$ and an average of $\langle \cos \theta \rangle \approx 0.8$. The average muon energy is $\langle E_\mu \rangle \approx 270 \text{ GeV}$ [20, 21]. Muons which have reached CUORE – and have not interacted in or near the detector so as to induce an electromagnetic shower – will deposit energy in a track-like manner as they traverse the crystals of the detector. The energy deposited in an individual crystal will be related to both the track-length travelled, along with fluctuations intrinsic to the processes of energy loss within media. Muons reaching LNGS are typically close to minimally-ionizing particles, with most probable energy losses on the order of a few $\text{MeV} \cdot \text{g}^{-1} \cdot \text{cm}^{-2}$.

124 **3 Multi-Objective Optimization**

125 The segmented nature of the CUORE detector makes track reconstruction difficult. The detector
126 is relatively small and with coarse spatial segmentation compared to a typical muon tracker. As
127 a starting-place, consider a naive unweighted Least Squares (LSQ) algorithm for reconstructing a
128 track direction, \hat{v} , given by the minimization of

129
$$g(\hat{v}) := \min_{\{\alpha_i\}} \sum_{i=1}^n \|\vec{x}_i - \bar{x} - \alpha_i \hat{v}\|^2 \quad (3.1)$$

130 subject to the constraint $\|\hat{v}\| = 1$. Here, the sum is over the crystals registering energy depositions
131 ("lit" channels), \vec{x}_i denotes the center of the i^{th} crystal, \bar{x} is the spatial average over "lit" crystal
132 centers, and $\{\alpha_i\}$ is a possible set of distances from the track to the n "lit" crystals. This minimizes
133 the total sum of squared distances between the reconstructed track and the centers of all "lit" crystals,
134 and \hat{v} may be efficiently computed as the first principle-component direction of the locations of the
135 "lit" crystal centers.

136 As we will demonstrate later, this naive LSQ fit tends to be biased towards pulling the recon-
137 structed track towards the crystal centers rather than toward the true track. Additionally, this LSQ
138 fit is susceptible to outliers, for example an accidental (uncorrelated) coincidence which may be
139 far from the track and pull the reconstructed track accordingly. It also does not utilize additional
140 information such as the positions of crystals which did *not* detect any energy, or the specifics of
141 the energy deposited in each crystal. A more robust track reconstruction algorithm would take
142 advantage of all the available information and treat the detector as a whole rather than focusing only
143 on the channels where energy was detected.

144 The algorithm that we propose here attempts to find a track that optimizes the channels where
145 energy is detected, the "lit channels," the channels where no energy is detected, the "unlit channels,"
146 as well as the best estimate of the energy that was deposited in each lit channel. Defining a generic
147 optimization of these three features in any given event is non-trivial due to the geometry of the
148 CUORE detector. For example, it is not obvious how to quantitatively weight fitting the lit channels
149 in any particular event against fitting the unlit channels. This weighting may depend on the direction
150 of the track and the path the track takes through the detector. In this work we do not attempt to
151 model it.

152 Multi-objective optimization describes a class of optimization techniques which aim to optimize
153 several objective functions simultaneously. This is often useful when the relative importance
154 between the objectives are uncertain or poorly defined. By optimizing simultaneously, a multi-
155 objective optimization process searches the space of possible trade-offs between the objectives.
156 Often, the outcome of an optimization of n objectives is an $(n - 1)$ -dimensional "Pareto front",
157 defining the subspace of optima for all possible weightings of the defined objectives.

158 In the algorithm presented here, we found that minimizing over three particular cost functions
159 was able to reproduce simulated tracks with good reliability. The motivation for each of the
160 functions came from a corresponding property of the track to be optimized for. The first two cost
161 functions are meant to only consider geometrical information for characterizing a track. The first
162 two objective functions assign costs on the basis of whether a candidate trajectory has intersected
163 as many "lit" crystals as possible (in the case of the first objective), or has minimized the number of

"unlit" crystals as much as possible (in the case of the second objective). The first two objectives are designed to be computationally efficient approximations to crystal intersections by approximating a crystal intersection with a logistic function, defined separately for "lit" and "unlit" crystals. The resulting objectives take the form

$$f_{1,2}(x) = \sum_{i \in \Omega_{1,2}} \frac{1}{1 + e^{\lambda_{1,2}(x_i - \alpha_{1,2})}}. \quad (3.2)$$

where x_i is the minimum distance between the i^{th} crystal center and the reconstructed track, $\alpha_{1,2}$ encodes a geometric "crystal size" (described below), and $\lambda_{1,2}$ defines the "sharpness" of the crystal edge.

The first objective encourages track collisions with all "lit" crystals. The parameters are given by $\lambda_1 = -.2 \text{ mm}^{-1}$ and $\alpha_1 = 25\sqrt{3} \text{ mm}$, where $25\sqrt{3} \text{ mm}$ is an upper bound on the distance within which a collision could occur (the distance between a crystal center and corner), such that the logistic function returns a penalty close to 1 if the track lies outside of the crystal, and close to 0 penalty if inside. The sum i is taken over all "lit" crystals, Ω_1 .

Conversely, the second objective function encourages avoidance of track collisions with all "unlit" crystals by taking an average of crystal costs and setting $\lambda_2 = .2 \text{ mm}^{-1}$ and $\alpha_2 = 25 \text{ mm}$, where 25 mm is a lower bound on the distance from which a track misses a crystal. The sum i is taken over all "unlit" crystals, Ω_2 . For both objectives, $\lambda_{1,2}$ was chosen phenomenologically to give reasonable algorithm performance, but may be further tuned in the future to improve performance.

Lastly, the third objective function encourages dE/dx values with high probability given a particle of interest. The geometric path length through each intersected is calculated by performing line-plane intersections. The probability densities are then computed from a PDF given by GEANT4, from which a log-likelihood based cost is returned:

$$f_3(x) = - \sum_i \log(p(\beta_i)) \quad (3.3)$$

where β_i gives the calculated dE/dx of the candidate trajectory through the i^{th} crystal based in its reconstructed energy E_i and path length l_i ,

$$\beta_i = E_i / L_i, \quad (3.4)$$

and p gives the probability density function (PDF) of β for a given particle (see Fig. 3). The sum i runs over crystals that are intersected by the proposed track with non-zero energy depositions, and crystals which are deemed to have been saturated are excluded from this objective function on account of providing unreliable energy information. In future versions of the algorithm, False-Hits and False-Misses could be incorporated into this sum.

Once these objectives are defined, a two tiered optimization process begins, utilizing two algorithms from the Multi-objective Optimization python library pyMOO [23]: NSGA-II [24] and NSGA-III [25–27]. NSGA-II (for two objectives) and NSGA-III (for three or more) are genetic algorithms, beginning with some initial population of size n and evolving population members where survival is determined from the objective costs, forming the Pareto front. The algorithm terminates after the completion of a number of evolutionary steps. The first tier begins with NSGA-II, optimizing trajectories over f_1 and f_2 . The initial population is defined as a random sample over

202 the sample space, where trajectories over the sample space are constrained to intersect with at least
203 two crystals which are closest to the LSQ fit line. The outcome is a Pareto front representing the best
204 trajectory candidates by strictly geometrical considerations, which is a sample of those trajectories
205 which intersect with the most "lit" crystals, the fewest "unlit" crystals, and the range of trade-offs in
206 between.

207 Members of the Pareto front produced from NSGA-II are then defined as the initial population
208 for which NSGA-III will optimize, but now with consideration of f_3 in addition to f_1 and f_2 . Once
209 termination is reached, a selection from the Pareto front is made according to the following scheme:

- 210 1. Compute which crystals were intersected for each candidate track using the line-cube collision.
- 211 2. Keep the track candidates which intersect the most "lit" crystals;
- 212 3. Among these, keep only the track candidates that intersect the fewest number of "unlit"
213 crystals;
- 214 4. Select from remaining according to the lowest f_3 cost (picking randomly for tie-breaking).

215 Multi-objective optimization of these cost functions together provide a number of advantages
216 over an LSQ algorithm. First, the approach is more robust to outliers, such as accidental coincident
217 events. For instance, a randomly coincident event located far from a trajectory could pull the
218 estimated trajectory given by an LSQ to be closer to that of the coincident event, whereas the cost
219 of the given objective functions will have no effect on the MO optimization, uniformly raising the
220 costs of all track candidates by a constant. Moreover, much more information is utilized in the
221 fitting of a track, such as the full 3-dimensional geometries of individual crystals and the overall
222 array, as well as information about energy depositions which would be neglected in a naive LSQ
223 fitting.

224 Lastly, by optimizing over f_3 , tracks whose energy deposition profile has high likelihood given
225 its corresponding dE/dx PDF are searched for. The likelihood from the best tracks can then be used
226 to perform hypothesis testing on the type of particle detected. This is discussed further in Sec. 6.

227 In experimental data we expect that secondary scattered particles will occasionally deposit
228 energy in crystals that are near to, but not intersected by the primary particle trajectory. These
229 secondary crystals are not accounted for in the current fit, but could be accounted for in future
230 versions. It is worth pointing out that the MOO algorithm is robust to outlier crystals, so the
231 impact on track reconstruction is expected to be small. Large showering events—such as a muon
232 that produces a hadronic shower—that are not well described as a track are rare, and are beyond the
233 scope of this work.

234 4 Simulation of Muon Tracks

235 In this algorithm, we use two Monte-Carlo (MC) simulations: a toy MC to quickly calculate
236 trajectories and geometric intersections, and a GEANT4-based MC [28] to understand the energy
237 deposition within a single crystal.

238 Since each step of the optimization requires testing the crystal intersections of a proposed track,
239 we designed a toy MC to simulate tracks through the CUORE detector. We construct the CUORE

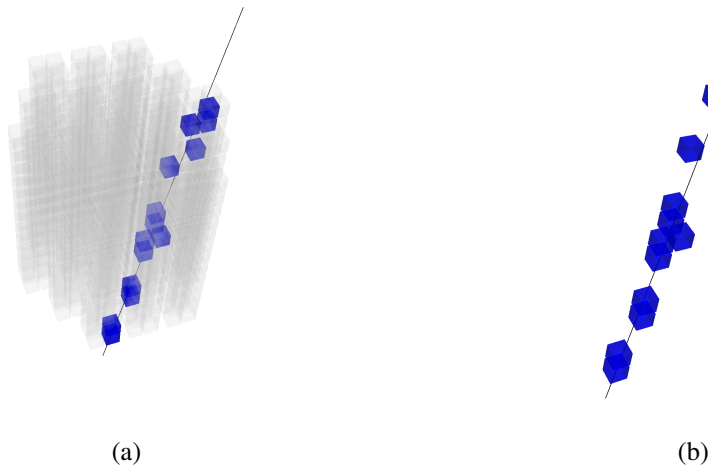


Figure 2: Simulated particle trajectories from the toy MC. Left: Trajectory through the entire CUORE array. Intersected crystals are highlighted in blue. Crystals are rendered transparent for clarity. Right: Same trajectory but isolating only the intersected crystals.

detector geometry, including the coordinates of each crystal and its dimensions, excluding support structures and shields. We simulate a track by defining an origin point within the detector and a direction. Each track may contain intersected crystals (e.g. shown in Fig. 2). Given a chosen trajectory, we then calculate the geometric path length through each intersected crystal.

To validate our optimizer, we use the toy MC simulation to build a population of tracks to fit. In this case the toy MC creates a large sample of tracks and takes the additional step of converting path lengths into energy depositions. The energy deposition in a crystal is chosen by randomly sampling the dE/dx PDF of that particle and multiplying by the path length. The dE/dx PDF is taken from the Geant4 simulation described below. The toy MC simulations do not generate secondary showering particles, which are discussed further below.

A GEANT4 simulation was used for calculating dE/dx curves by sampling trajectories of particles of interest through a single $5\text{ cm} \times 5\text{ cm} \times 5\text{ cm}$ cube of TeO_2 . A particle is simulated at a random point on the surface with a random direction into the crystal. For a given trajectory, we calculate the path length it took through the crystal, as well as the total energy deposited in the crystal over the path, allowing us to approximate dE/dx as in Eqn. 3.4. Performing this calculation over all sample trajectories, we are left with a dE/dx distribution shown in Fig. 3.

In practice, detectors have finite energy resolution and dynamic range. For example, the CUORE bolometers are designed for energy depositions around a few MeV, and may saturate for a muon energy deposition above a few 10s of MeV. To evaluate the impact this behavior might have on the algorithm's performance we perform simulations with finite energy resolution and energy saturation. We refer to our baseline simulations with perfect energy resolution and no saturation as the "Perfect Energy" simulations. We also consider the following configurations:

- "Saturation": This conservative configuration assumes a 10 keV full-width-at-half-maximum (FWHM) energy resolution up to 20 MeV, with energy depositions above 20 MeV saturating and assigned the maximum value of 20 MeV.

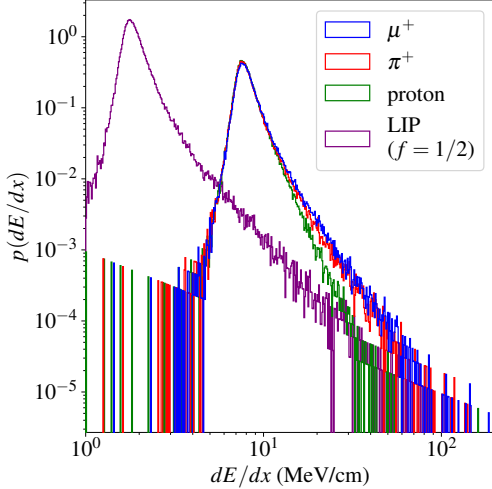


Figure 3: Distribution of simulated dE/dx values in a $5\text{ cm} \times 5\text{ cm} \times 5\text{ cm}$ TeO_2 crystal for 300 GeV muons, protons, pions, and a hypothetical muon-like LIP with charge $e/2$. (LIP simulation used modifications to Geant4 from the FCP_Simulation package [29, 30].) Interestingly, an individual crystal of this size is not able to distinguish between muons, pions and protons via dE/dx .

- "Finite Resolution": This slightly more optimistic configuration assumes that energy depositions above the saturation energy can be recovered with some kind of fit extrapolation, but at the cost of a worse energy resolution. As in the "Saturation" configuration, we assume an energy resolution of 10 keV FWHM up to 20 MeV but assume a 10% FWHM resolution above 20 MeV.

Unless otherwise indicated, results discussed are based on the "Perfect Energy" simulations.

5 Algorithm Performance on Muon Tracks

We test our algorithm's performance on a sample of 7324 muons generated using the MC simulations described in the previous section. We compare our algorithms performance to the performance of a naive LSQ algorithm (as previously described) as a benchmark.

We assess the algorithm's ability to accurately reconstruct the original trajectory of a particle to which it was blind. The algorithm takes only the simulated energy depositions, as it would in the case of real data. As mentioned, one motivation for the multi-objective approach was to include distinct objectives for considering crystal collisions in the trajectory. The consideration of collisions creates two categories of error crystals: 1) False-Hits: crystals which were intersected by the reconstructed trajectory but which did not detect any energy depositions. 2) False-Misses: crystals which detected energy depositions but were not intersected by the reconstructed trajectory.

In Fig. 4, we show a comparison between performance of a naive LSQ against the multi-objective algorithm over False-Hits and False-Misses. On this sample our algorithm was able to increase the number of reconstructions with no False-Hits from 34% to 74%. It was similarly able to increase the number of reconstructions with no False-Misses from 75% to 97%. These statistics are

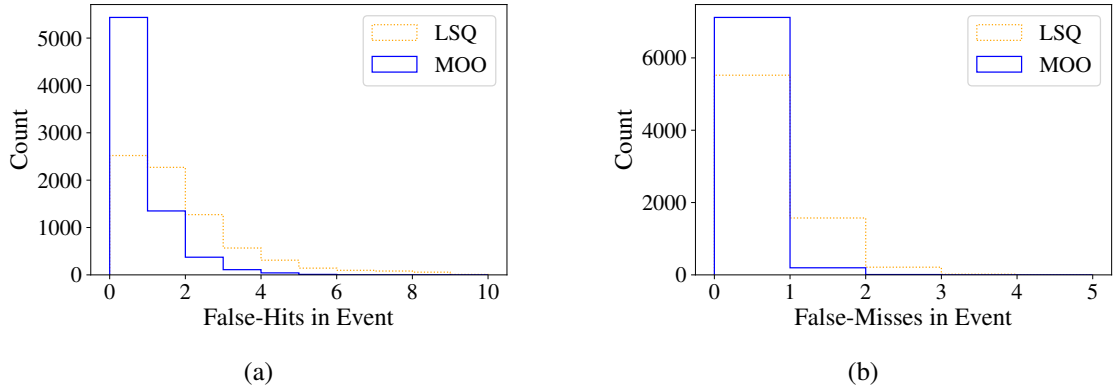


Figure 4: Distribution of error crystals for Multi-Objective Optimization (MOO) compared to least squares. Left: Distribution of number of false-hit crystals. Right: Distribution of false-missed crystals. The MOO algorithm out performs the naive LSQ algorithm in terms of both false-hit and false-missed crystals.

particularly important for delayed coincidence analyses to look for cosmogenic crystal activation, which rely on an accurate accounting of which crystals have been struck.

Pointing accuracy of reconstructed trajectories is calculated by finding angular separations from the corresponding true trajectory. Fig. 5d shows a comparison of distributions of pointing accuracy between our algorithm and least squares, while Fig. 5 shows the specific performance in the azimuthal and zenith angles. The average angular error was reduced between the methods from 2.55 degrees for LSQ to 1.81 degrees for MOO.

Additionally, we assess the ability of the algorithm to reconstruct path-lengths on the individual crystal level. The ability for this to be done accurately is of critical importance for calculating dE/dx and thus for assessing the probability for a particular trajectory. This probability is taken into account in the third objective function mentioned in Sec. 3, and could also be useful in hypothesis testing. As shown in Fig. 6, we compare the path-length reconstruction between our algorithm and LSQ over the $\sim 63,000$ intersected crystals from the same sample of simulated muons. We saw mean square error improvement by a factor of 2.5 as well as an r^2 increase from .48 to .79.

The change in structure at 50 mm within Figure 6 for the LSQ fits also reveals how bias within the LSQ algorithm pulls tracks to pass close to the crystal centers. Regardless of the true path-length, the LSQ algorithm prefers to reconstruct through-going tracks with path-lengths greater than the crystal side-length of 50 mm, as compared to "glancing" hits with path-lengths less than the side-length. Comparatively, the MOO algorithm can reliably reconstruct short path-lengths which lie far from the crystal center.

Finally, we consider the impact on pointing accuracy coming from the detector-response effects of energy resolution and crystal saturation. As described in Sec. 4, we evaluate the MOO performance on the conservative "Saturation" simulations and the slightly more optimistic "Finite Resolution" configuration. Comparing the results of the "Perfect Energy", "Saturation," and "Finite Resolution" simulations, we find as would be expected that the algorithm performs worse when energy resolution and saturation effects are included, with Table 1 providing the mean and standard deviations in reconstructing the single-crystal track lengths and overall pointing accuracy. However,

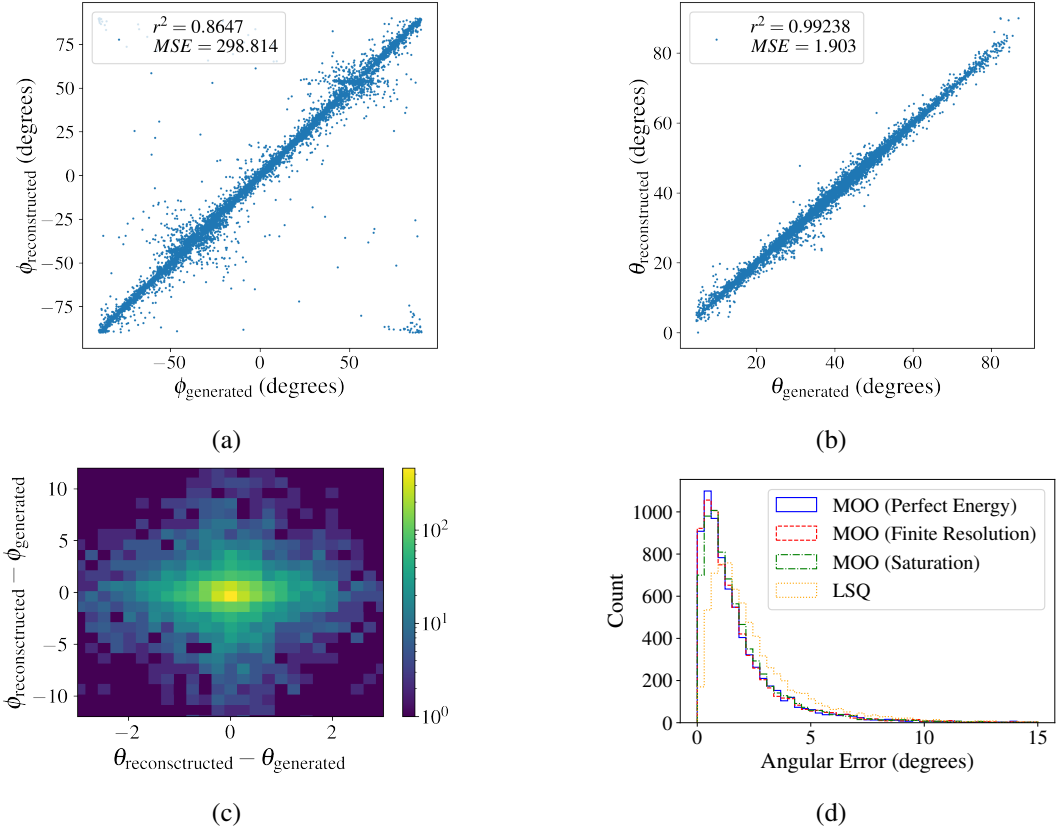


Figure 5: Algorithm performance of direction reconstruction. (a) Azimuthal reconstruction, (b) Zenith reconstruction, (c) Correlated azimuth vs zenith (both angles in degrees), (d) absolute pointing error. The increased scatter in the azimuthal reconstruction around $\phi \approx -30^\circ, 60^\circ$ are due to the alignment of tracks with crystal planes in the CUORE detector and are particular to the symmetries of that geometry.

the degradation in pointing accuracy as shown in Fig. 5d and other metrics is rather minor, with mean pointing accuracy increasing by only 4.4% for the "Saturation" and 0.5% for the "Finite Resolution" simulations over the idealized "Perfect Energy" data set. Furthermore, the MOO algorithm on both "Saturation" and "Finite Resolution" simulations still far outperform the LSQ algorithm's performance.

In Fig. 7, we show the algorithm evaluated on two track-like events from real CUORE data that are presumed to be muons. The events contain saturated pulses whose energy is poorly measured by the current reconstruction algorithms. Of course, the true track is unknown, however, the algorithm correctly explains the saturation of channels based on the reconstructed path length. This is clearly a direction for future research.

6 Discussion

The CUORE detector is optimized for the search for neutrinoless double-beta decay, which largely treats each calorimeter individually or in an anti-coincidence mode. The algorithm presented

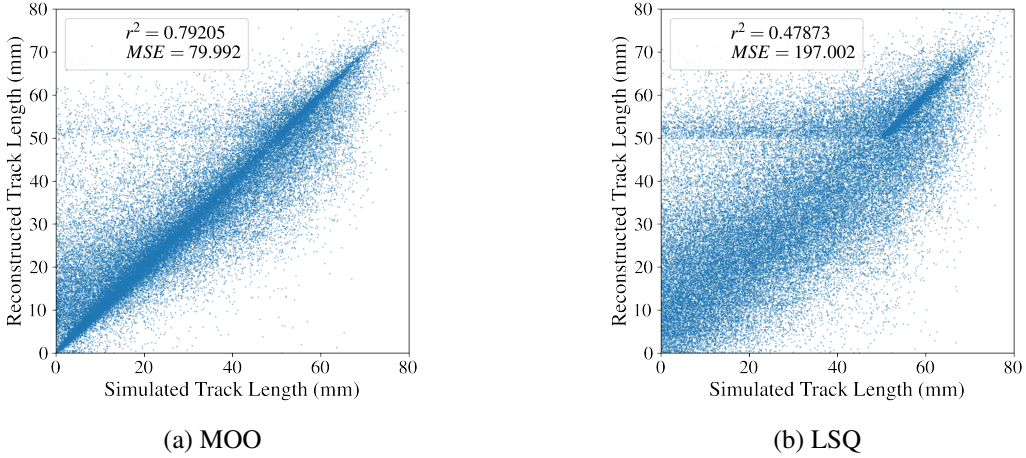


Figure 6: Distribution of crystal path-length reconstructions for MOO (left) compared to LSQ (right). The tighter clustering around $y = x$ for the MOO indicates a much more reliable reconstruction of the path length through each crystal, yielding a higher correlation coefficient r^2 and a lower Mean Squared Error (MSE).

Table 1: Means and standard-deviations (σ) for the MOO and LSQ algorithms in reconstructing single-crystal track lengths and overall pointing accuracy.

| Algorithm | Δ (Track Length) (mm) | | Pointing Accuracy (°) | |
|-------------------------------|------------------------------|----------|-----------------------|----------|
| | Mean | σ | Mean | σ |
| MOO ("Perfect Energy") | 5.18 | 7.28 | 1.81 | 2.05 |
| MOO ("Finite Resolution") | 5.20 | 7.29 | 1.82 | 2.08 |
| MOO ("Saturation") | 5.93 | 7.95 | 1.89 | 2.00 |
| LSQ ("Perfect Energy Energy") | 9.72 | 10.12 | 2.55 | 2.21 |

here expands the CUORE analysis infrastructure to better reconstruct track-like muons, treating the detector holistically as a segmented detector. The crystal coarseness and lack of time-of-flight information for relativistic particles makes track-reconstruction more difficult compared to dedicated tracking detectors, nonetheless the MOO-based algorithm presented here is able to overcome such limitations in reconstructing track paths.

Comparisons to the "naive" LSQ-based reconstruction highlight some of the potential issues that can manifest when fitting to coarsely segmented tracks. The LSQ algorithm serves not only as a benchmark with which to compare the improvements of the MOO-based approach, but also indicates that the sophistication of the MOO algorithm is necessary to avoid issues arising from the discreteness of triggered channels, and eliminate the bias towards crystal centers that may generally arise when fitting to a single spatial/energy-weighted objective function. Moreover, the MOO algorithm still demonstrates strong performance under the presence of imperfect detector response effects such as crystal saturation and finite energy resolution.

Preliminary validation of the algorithm's performance may be evaluated within physics data collected by CUORE by looking at channel saturation within tracks. Up to fluctuations in dE/dx

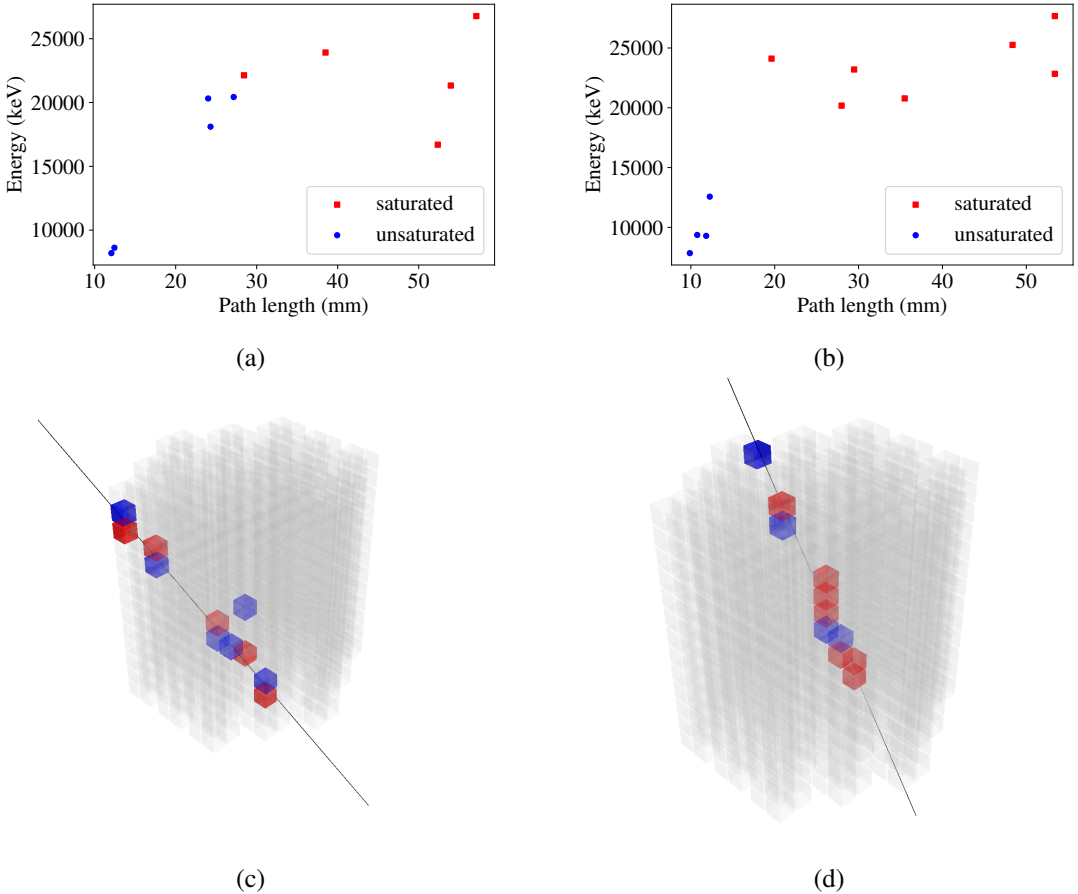


Figure 7: Top: Two track-like events from CUORE (left and right), that are presumed to be muons. Each point in the plot corresponds to a single lit crystal in the track. The crystal track lengths reconstructed by the MOO algorithm are plotted on the x-axis, with the reconstructed energy (from the CUORE data processing) plotted along y. The reconstructed energies are inputs into the MOO algorithm and the crystal track lengths are outputs. The saturation energy varies between the CUORE calorimeters but is typically around 20 MeV – above saturation the reconstructed energy can be very inaccurate. The MOO algorithm explains the calorimeter saturation by the long reconstructed track lengths. Bottom: A geometric visualization of the same tracks. The blue and red color coding corresponds to non-saturated and saturated crystals, respectively.

related to the energy loss of the primary particle, energy deposition within crystals is expected to be linearly proportional to the pathlength traversed. Channels within CUORE have typical saturation energies of 20 MeV, meaning for that for muons with most-probably energy-depositions of ~ 10 MeV/cm in TeO_2 , path-lengths through a crystal greater than ~ 2 cm have a high probability of saturating that channel. Figure 7 showing crystal energy versus reconstructed path-lengths for probable muon tracks identified within CUORE physics data, showing the expected linear relationship between path-length and energy, up until crystal saturation begins to take place for path-lengths greater than ~ 2 cm, as expected.

Further studies on CUORE data using this algorithm will provide a greater understanding

350 of muons within the detector. While the muon rate within CUORE is efficiently reduced by
351 its depth within LNGS, of particular interest is the investigation into any remaining cosmogenic
352 activation of nuclides which can constitute backgrounds to searches for neutrinoless double beta
353 decay. Application of this algorithm will also be useful for the CUPID upgrade to CUORE, which
354 plans to include a dedicated muon veto surrounding the detector [31].

355 While much of this work has considered track-like muon events, the algorithm presented can be
356 adapted to perform searches for exotic track-like events within CUORE. It is worth noting that due
357 to the relatively small crystal size and large fluctuations in energy deposition, it is not possible to
358 distinguish between relativistic Standard Model (SM) particles such as muons, pions, and protons
359 (see Fig. 3). But Beyond Standard Model (BSM) particles such as low-velocity monopoles [32–
360 36], LIPs [37–41], and multiply-interacting dark matter (MIDM) [42] are all predicted to produce
361 track-like energy depositions with a substantially different dE/dx compared to muons, pions, and
362 protons. By adjusting the dE/dx PDF within the f_3 objective searches for such BSM-particles can
363 be conducted, with the likelihood ratio $f_3^{\text{BSM}}/f_3^{\text{muon}}$ being a suitable test statistic for discriminating
364 BSM candidates from background muons. We leave sensitivity predictions for such searches for
365 future work.

366 While this algorithm was developed with the CUORE detector and geometry in mind, it is
367 important to note that it is easily transferred to other segmented detector arrays. The logistic
368 regression hyperparameters α and λ within the "hit" and "missed" channel objective functions
369 may easily be tuned using simulated data for an arbitrary detector geometry, while the rest of the
370 algorithm is based on the full geometric implementation of the detector array. To recall, such
371 hyperparameters are necessary for smoothing the objective functions while the algorithm evolves
372 to find the Pareto front. Importantly, they are not used in the final track selection across the Pareto
373 front, which instead utilizes the full analytic calculation of crystal-track intersections.

374 Other future directions for improvement to the algorithm presented here include extracting
375 event-level uncertainties and accounting for correlated nearby channels. Event-level uncertainties
376 could be extracted from one or more of the cost functions, but this is made slightly complicated
377 by the fact the MOO by definition does not combine the costs into a single function that could act
378 as a "likelihood". Muons and other high energy events can produce secondaries that could deposit
379 energy into channels that are not directly intersected by the track. This could include low-energy
380 secondaries like Bremsstrahlung photons or high-energy ones like annihilation γ 's. These correlated
381 off-track channels are currently treated in the same manner as an accidental coincidence, but could
382 be incorporated into the cost functions in the future to further improve event reconstruction. Finally,
383 the algorithm could potentially be generalized to fit multiple simultaneous tracks e.g. from muon
384 shower events.

385 Acknowledgments

386 The authors would like to thank the CUORE Collaboration for useful conversations, in particular,
387 Jorge Torres, Erin Hansen, Douglas Adams and Thomas O'Donnell. Further, we thank the CUORE
388 Collaboration for the use of the CUORE muon events, which made use of the DIANA data analysis and
389 APOLLO data acquisition software which has been developed by the Cuoricino, CUORE, LUCIFER,

390 CUPID-0, and CUPID-Mo Collaborations. This work was funded by the US Department of Energy,
391 Office of Science, Office of Nuclear Physics under grant number DE-SC0011091.

392 References

- 393 [1] M. Clark et al., *Direct detection limits on heavy dark matter*, *Phys. Rev. D* **102** (Dec, 2020) 123026.
- 394 [2] SUPERCDMS COLLABORATION collaboration, I. Alkhateb et al., *Constraints on Lightly Ionizing*
395 *Particles from CDMSlite*, *Phys. Rev. Lett.* **127** (Aug, 2021) 081802.
- 396 [3] MAJORANA COLLABORATION collaboration, S. I. Alvis et al., *First limit on the direct detection of*
397 *lightly ionizing particles for electric charge as low as e/1000 with the majorana demonstrator*, *Phys.*
398 *Rev. Lett.* **120** (May, 2018) 211804.
- 399 [4] S. Cebrián, *Cosmogenic activation in double beta decay experiments*, *Universe* **6** (Sep, 2020) 162.
- 400 [5] C. Zhang, D.-M. Mei, V. Kudryavtsev and S. Fiorucci, *Cosmogenic activation of materials used in*
401 *rare event search experiments*, *Astroparticle Physics* **84** (2016) 62–69.
- 402 [6] B. S. Wang et al., *Cosmogenic-neutron activation of TeO₂ and implications for neutrinoless double-β*
403 *decay experiments*, *Phys. Rev. C* **92** (2015) 024620, [[1503.02095](#)].
- 404 [7] CUORE collaboration, D. Q. Adams et al., *Improved Limit on Neutrinoless Double-Beta Decay in*
405 *¹³⁰Te with CUORE*, *Phys. Rev. Lett.* **124** (2020) 122501, [[1912.10966](#)].
- 406 [8] CUORE collaboration, D. Q. Adams et al., *Measurement of the 2νββ Decay Half-Life of ¹³⁰Te with*
407 *CUORE*, *Phys. Rev. Lett.* **126** (2021) 171801, [[2012.11749](#)].
- 408 [9] CUORE collaboration, D. Q. Adams et al., *Search for majorana neutrinos exploiting millikelvin*
409 *cryogenics with CUORE*, *Nature* **604** (2022) 53–58.
- 410 [10] C. Alduino et al., *The cuore cryostat: An infrastructure for rare event searches at millikelvin*
411 *temperatures*, *Cryogenics* **102** (2019) 9–21.
- 412 [11] “CUORE Public Website.” <https://cuore.lngs.infn.it/>.
- 413 [12] E. E. Haller, N. P. Palaio, M. Rodder, W. L. Hansen and E. Kreysa, *NTD Germanium: A Novel*
414 *Material for Low Temperature Bolometers*, pp. 21–36. Springer US, Boston, MA, 1984.
415 10.1007/978-1-4613-2695-3_2.
- 416 [13] C. Arnaboldi et al., *A front-end electronic system for large arrays of bolometers*, *J. Instrum.* **13** (feb,
417 2018) P02026–P02026.
- 418 [14] S. D. Domizio et al., *A data acquisition and control system for large mass bolometer arrays*, *J.*
419 *Instrum.* **13** (dec, 2018) P12003–P12003.
- 420 [15] CUORE collaboration, C. Alduino et al., *Analysis techniques for the evaluation of the neutrinoless*
421 *double-β decay lifetime in ¹³⁰Te with the CUORE-0 detector*, *Phys. Rev. C* **93** (2016) 045503,
422 [[1601.01334](#)].
- 423 [16] C. Alduino et al., *Analysis techniques for the evaluation of the neutrinoless double-β decay lifetime in*
424 *¹³⁰Te with the cuore-0 detector*, *Phys. Rev. C* **93** (Apr, 2016) 045503.
- 425 [17] M. Redshaw, B. J. Mount, E. G. Myers and F. T. Avignone, *Masses of ¹³⁰Te and ¹³⁰Xe and*
426 *double-β-decay q value of ¹³⁰Te*, *Phys. Rev. Lett.* **102** (May, 2009) 212502.
- 427 [18] N. D. Scielzo et al., *Double-β-decay q values of ¹³⁰Te, ¹²⁸Te, and ¹²⁰Te*, *Phys. Rev. C* **80** (Aug, 2009)
428 025501.

- 429 [19] S. Rahaman et al., *Double-beta decay q values of 116cd and 130te*, *Phys. Lett. B* **703** (2011) 412–416.
- 430 [20] MACRO collaboration, S. P. Ahlen et al., *Muon astronomy with the MACRO detector*, *Astrophys. J.*
431 **412** (1993) 301–311.
- 432 [21] LVD COLLABORATION collaboration, M. Aglietta et al., *Muon “depth-intensity” relation measured by*
433 *the LVD underground experiment and cosmic-ray muon spectrum at sea level*, *Phys. Rev. D* **58** (Oct,
434 1998) 092005.
- 435 [22] F. Bellini, C. Bucci, S. Capelli, O. Cremonesi, L. Gironi, M. Martinez et al., *Monte carlo evaluation*
436 *of the external gamma, neutron and muon induced background sources in the cuore experiment*,
437 *Astroparticle Physics* **33** (2010) 169–174.
- 438 [23] J. Blank and K. Deb, *Pymoo: Multi-Objective Optimization in Python*, *IEEE Access* **8** (2020)
439 89497–89509.
- 440 [24] K. Deb, A. Pratap, S. Agarwal and T. Meyarivan, *A fast and elitist multiobjective genetic algorithm:*
441 *NSGA-II*, *IEEE Trans. Evol. Comput.* **6** (2002) 182–197.
- 442 [25] K. Deb and H. Jain, *An Evolutionary Many-Objective Optimization Algorithm Using*
443 *Reference-Point-Based Nondominated Sorting Approach, Part I: Solving Problems With Box*
444 *Constraints*, *IEEE Trans. Evol. Comput.* **18** (2014) 577–601.
- 445 [26] H. Jain and K. Deb, *An Evolutionary Many-Objective Optimization Algorithm Using Reference-Point*
446 *Based Nondominated Sorting Approach, Part II: Handling Constraints and Extending to an Adaptive*
447 *Approach*, *IEEE Trans. Evol. Comput.* **18** (2014) 602–622.
- 448 [27] J. Blank, K. Deb and P. C. Roy, *Investigating the Normalization Procedure of NSGA-III*, in
449 *Evolutionary Multi-Criterion Optimization* (K. Deb, E. Goodman, C. A. Coello Coello, K. Klamroth,
450 K. Miettinen, S. Mostaghim et al., eds.), pp. 229–240, Springer International Publishing, 2019.
- 451 [28] S. Agostinelli et al., *Geant4 – a simulation toolkit*, *Nucl. Instrum. and Methods in Phys. Res. A* **506**
452 (2003) 250–303.
- 453 [29] S. Banik, V. Kashyap, M. Kelsey, B. Mohanty and D. Wright, *Simulation of energy loss of fractionally*
454 *charged particles using Geant4*, *Nucl. Instrum. Methods Phys. Res. A* **971** (2020) 164114.
- 455 [30] S. Banik, “FCP_Simulation.” https://github.com/SamirBanik/FCP_Simulation, 2019.
- 456 [31] CUPID collaboration, W. R. Armstrong et al., *CUPID pre-CDR*, [1907.09376](https://arxiv.org/abs/1907.09376).
- 457 [32] P. A. M. Dirac, *Quantised singularities in the electromagnetic field*, *Proc. R. Soc. Lond. A* **133** (1931)
458 60–72, [<https://royalsocietypublishing.org/doi/pdf/10.1098/rspa.1931.0130>].
- 459 [33] P. A. M. Dirac, *The Theory of Magnetic Poles*, *Phys. Rev.* **74** (Oct, 1948) 817–830.
- 460 [34] G. ’t Hooft, *Magnetic Monopoles in Unified Gauge Theories*, *Nucl. Phys. B* **79** (1974) 276–284.
- 461 [35] A. M. Polyakov, *Particle Spectrum in Quantum Field Theory*, *JETP Lett.* **20** (1974) 194–195.
- 462 [36] PARTICLE DATA GROUP collaboration, M. Tanabashi et al., *Review of particle physics*, *Phys. Rev. D* **98**
463 (Aug, 2018) 030001.
- 464 [37] S. L. Glashow and M. Gell-Mann, *Gauge theories of vector particles*, *Ann. Phys. (N. Y.)* **15** (1961)
465 437–460.
- 466 [38] A. Schellekens, *Electric charge quantization in string theory*, *Phys. Lett. B* **237** (1990) 363–369.
- 467 [39] E. Chun, A. S. Joshipura and A. Smirnov, *Models of light singlet fermion and neutrino*
468 *phenomenology*, *Phys. Lett. B* **357** (1995) 608–615.

- 469 [40] S. Abel, M. Goodsell, J. Jaeckel, V. Khoze and A. Ringwald, *Kinetic mixing of the photon with hidden*
470 *u(1)s in string phenomenology*, *J. High Energy Phys.* **2008** (jul, 2008) 124–124.
- 471 [41] C. Kouvaris, *Composite millicharged dark matter*, *Phys. Rev. D* **88** (Jul, 2013) 015001.
- 472 [42] J. Bramante, B. Broerman, R. F. Lang and N. Raj, *Saturated overburden scattering and the*
473 *multiscatter frontier: Discovering dark matter at the Planck mass and beyond*, *Phys. Rev. D* **98** (Oct,
474 2018) 083516.